Science Advances

AAAS

advances.sciencemag.org/cgi/content/full/2/11/e1600894/DC1

Supplementary Materials for

Superconducting topological surface states in the noncentrosymmetric bulk superconductor $PbTaSe_2$

Syu-You Guan, Peng-Jen Chen, Ming-Wen Chu, Raman Sankar, Fangcheng Chou, Horng-Tay Jeng,* Chia-Seng Chang,* Tien-Ming Chuang*

Published 23 November 2016, *Sci. Adv.* **2**, e1600894 (2016)
DOI: 10.1126/sciadv.1600894

The PDF file includes:

- fig. S6. BCS fitting of superconducting tunneling spectrum.
- fig. S7. Normalized differential conductance taken on Pb-terminated surface.
- fig. S8. Magnetic field dependence of superconducting vortex lattice and vortex bound states.
- fig. S9. Homogenous superconducting gap on a Pb-terminated surface.
- fig. S10. Topographic images of differential conductance maps on the Pb-terminated surface.
- fig. S11. Bias independence of LDOS mapping and QPI imaging.
- fig. S12. Raw data FFT of normalized differential conductance maps.
- fig. S13. Visualization of QPI at Fermi energy.

Other Supplementary Material for this manuscript includes the following:
(available at advances.sciencemag.org/cgi/content/full/2/11/e1600894/DC1)

- movie S1 (.mpg format). Normal-state QPI maps taken on a Pb-terminated surface.

Supplementary Materials

note S1. Crystal structures and electron diffraction patterns of $PbTaSe_2$.

It has been reported that $PbTaSe_2$ can crystallize in either $P6/mmm$ or $P\bar{6}m2$ symmetry (21, 25), both of which share identical x-ray reflection conditions. In reciprocal space, both structures readily show the same periodicity, hampering a clear separation of one from the other using associated diffraction techniques. In real space, the two structures are nonetheless distinctly different, with the phase of $P\bar{6}m2$ featuring a three-fold Ta network and that of $P6/mmm$ exhibiting six-fold but randomly distributed Ta atoms when observing along the c-axis. In the main text, Fig. 1B shows a typical *c*-projected HAADF image of $PbTaSe_2$, with the Ta network firmly exhibiting the three-fold character of $P\bar{6}m2$ and the overlaid Pb/Se atomic columns forming a continuous six-fold network. Fig. 1C illustrates the [110]-projected HAADF image of $PbTaSe_2$, showing the characteristic 1H-$TaSe_2$ cages of $P\bar{6}m2$. Our STEM results along with the STM topographic images on Se-surface confirm unambiguously that our $PbTaSe_2$ samples crystallize in $P\bar{6}m2$. The corresponding electron diffraction patterns are shown in fig. S1, free from any symmetry-forbidden reflections, demonstrating the appreciable structural perfection of our samples.

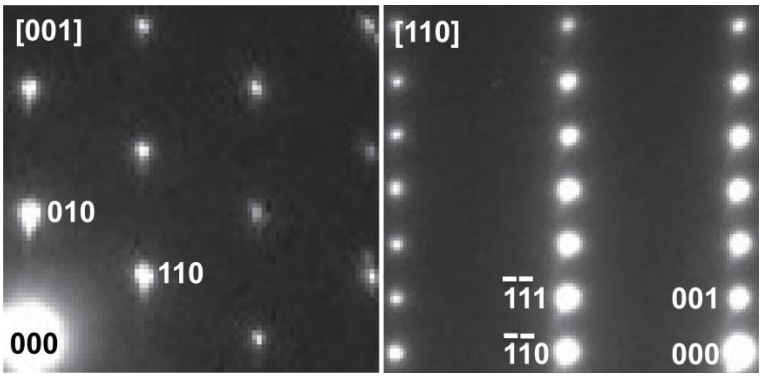

fig. S1. Electron diffraction patterns along [001] and [110] projection.

note S2. Spin-decomposed surface band structures of $PbTaSe_2$.

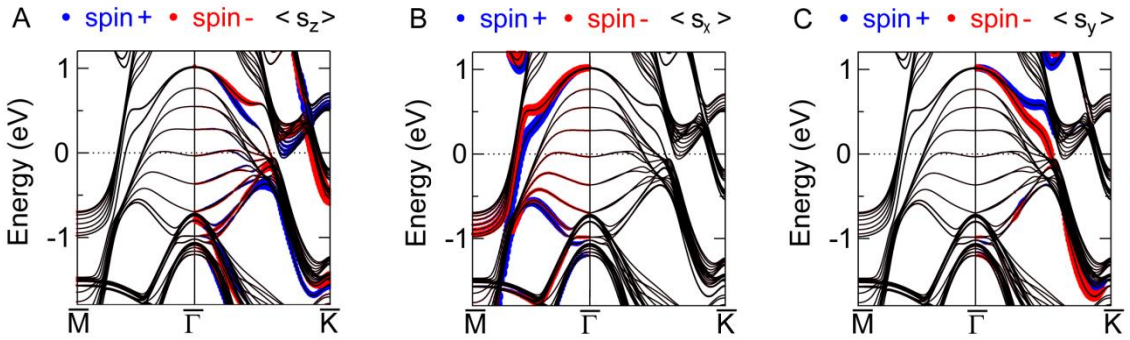

fig. S2. Projection of the spin polarizations of bands contributed from the surface atoms. (**A-C**) Projection along z, x and y direction, respectively.

note S3. The 2 × 2 superstructure on a Se-terminated surface.

The Se-surface exhibits a 2×2 superstructure in STM topographic images. In order to study the possibility of forming a superstructure, a 2×2 supercell with slightly displaced atoms is constructed. For Pb-terminated surfaces, the atoms move back to their original positions and restore the original 1×1 structure, consistent with the experimental observation that Pb-termination does not show a superstructure. While for Se-terminated surfaces, a new ground state arising from the tiny shift in Ta positions is found (fig. S3). The calculated results agree with the experimental observation that Se-termination shows a 2×2 superstructure while Pb-termination does not. The calculated atomic displacement pattern from also fits the STM topography. Three Ta atoms move toward one Se atom in 2×2 unit cells, shifting this Se atom upward slightly (fig. S3A). The shifted Se atoms show brighter contrast in topographic image. The atomic displacement of Ta atoms is ~0.07 Å and the energy gain is 2meV/Ta.

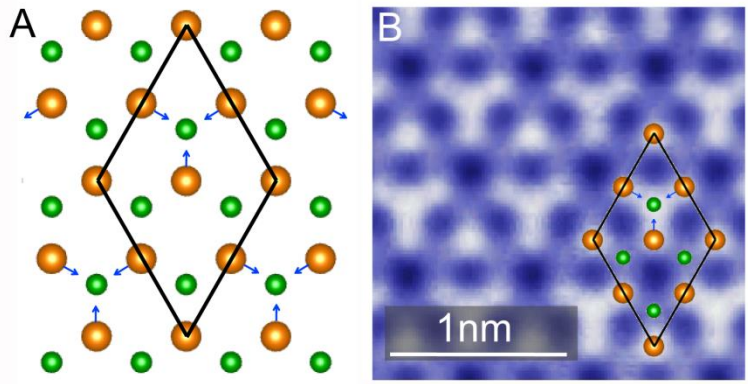

fig. S3. The simulated surface structure on the Se-terminated surface. (**A**) The black diamond represents a unit cell of 2x2 superstructure. The green and orange spheres represent Se and Ta atoms, respectively. The blue arrow indicates the in-plane movement of Ta atoms. (**B**) The $TaSe_2$ structure overlapped with a Se-terminated topographic image.

note S4. Verification of helical spin polarization in TSSs by QPI imaging.

For comparison with the measured QPI pattern, the autocorrelation is investigated via the nesting function

$$N(q,\varepsilon)=\frac{2}{N_k}\sum_{knm}\delta(\varepsilon_{k+qn}-\varepsilon)\delta(\varepsilon_{km}-\varepsilon)$$

where N_k is the number of k-points. As depicted in Fig. 1F, the outer TSS along $\overline{\Gamma K}$ with $E \lesssim 0.5eV$ has negligible components from the surface atoms because the strong overlapping with the bulk conduction bands. The length of the outer TSS in Fig. 4B and fig. S4A is estimated by the contribution of the surface atoms from the decomposed surface components (ranging from~80% at $\overline{M}$ to ~20% at $\overline{K}$) and the measured angular distribution of $\boldsymbol{q}_1$. Thus a window function is applied to suppress the contributions

from these states with ignorable surface components. The simulated dI/dV($\boldsymbol{q}$, E) images from the CEC at selected energies without (with) spin components are shown in fig. S4C and S4D (S4E and S4F).

The spin-dependence of QPI process is described by the inner product of the spin orientation $\boldsymbol{s}_1 \cdot \boldsymbol{s}_2$. Only two TSSs are taken into account in this calculation to reproduce the QPI patterns from SI-STM measurements. It is evident that more scattering processes are allowed when helical spin polarization is absent in TSS (fig. S4C and S4D). In contrast, the simulation taking into account the spin components of TSSs is in excellent agreement with measured QPI images (fig. S4E and S4F). Thus, our experiment results together with the QPI simulation support two TSSs are spin-polarized with opposite helical texture.

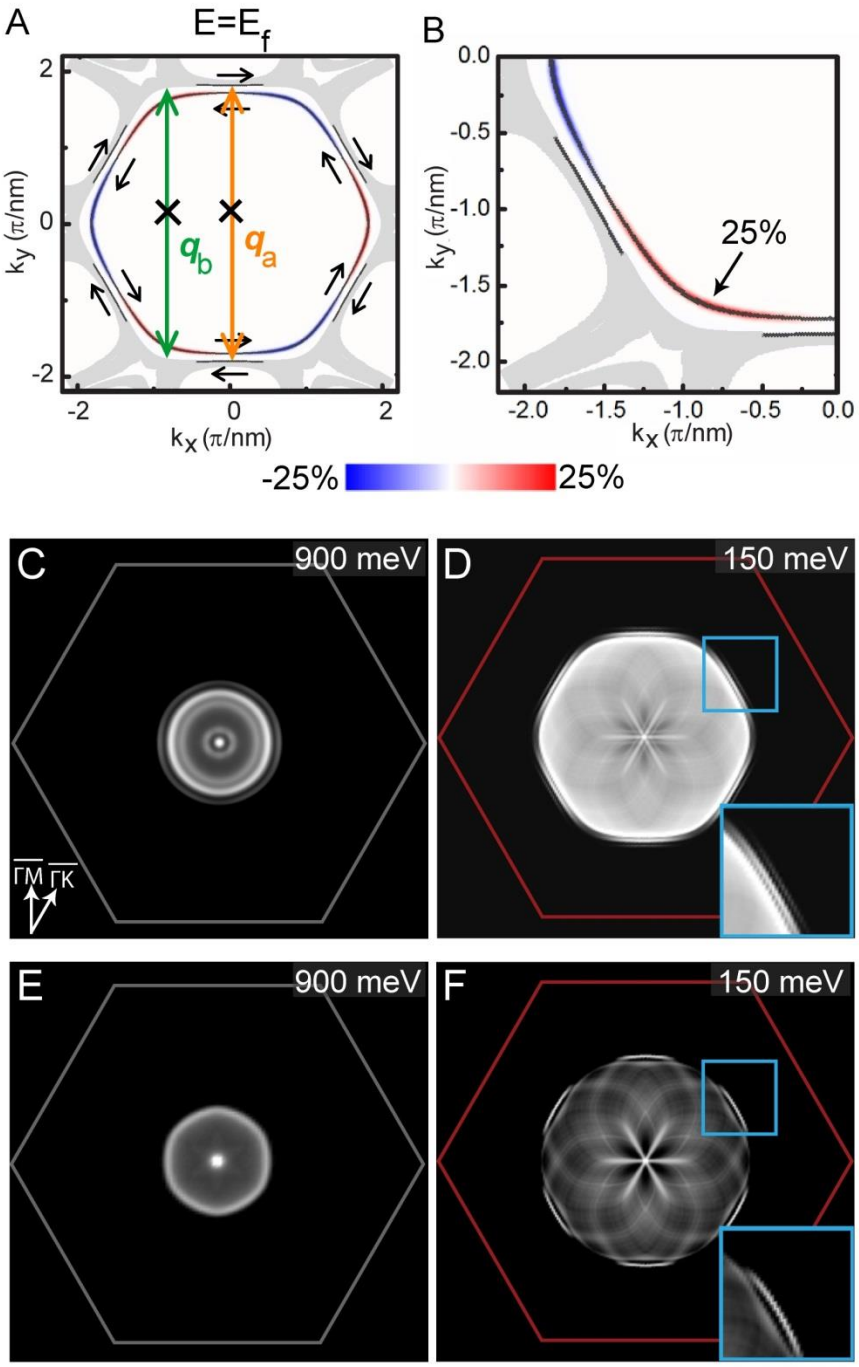

fig. S4. Spin-dependent QPI. (**A**) The calculated constant energy contour of two TSSs with spin texture at E_F. The black arrows represent the in-plane spin direction and the blue/red contours show the sign and the magnitude of out-of-plane spin. The gray shaped regions represent the calculated bulk conduction bands. Two possible intraband scattering processes ($\boldsymbol{q}_a$ and $\boldsymbol{q}_b$) are expected in addition to $\boldsymbol{q}_1$ and $\boldsymbol{q}_2$ in Fig. 4. $\boldsymbol{q}_a$ is forbidden because of opposite helical spin orientaion. $\boldsymbol{q}_b$ is not observed because of the overlapping between the bulk bands and the outer TSS in $\overline{\Gamma K}$ direction. (**B**) The zoom-in of (A). The QPI simulation (**C**)(**D**) without and (**E**)(**F**) with helical spin components. The gray and red hexagon indicates half and full Brillouin zone, respectively.

S5. Superconducting gap on Se-terminated surface.

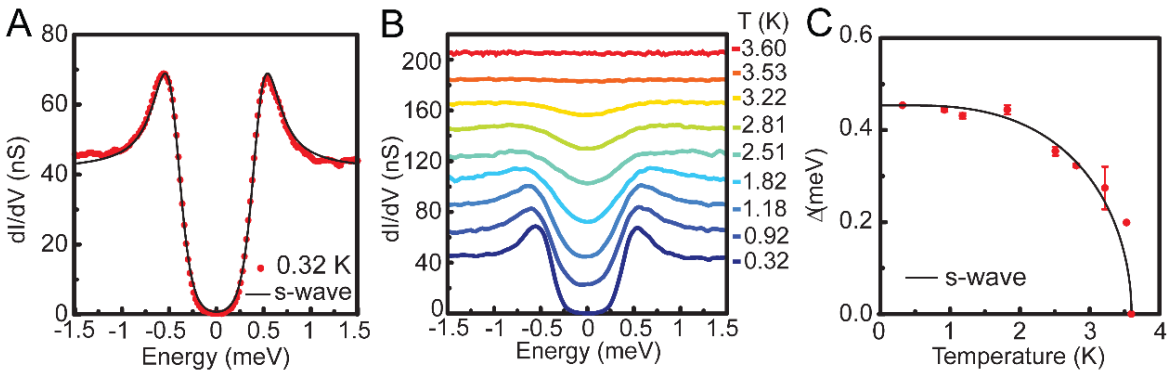

fig. S5. Temperature dependence of the superconducting gap. (**A**) The superconducting tunneling spectrum on Se-surface at 0.32 K. The black line is BCS fitting with Δ=0.45meV. (**B**) Temperature evolution of superconducting tunneling spectrum on Se-surface. The curves are equally shifted by 20nS for clarity. (**C**) Temperature dependence of superconducting gap. The black line is theoretical calculation using BCS theory for measured T_c = 3.6 K.

note S6. Single–s-wave gap and two–s-wave gap fitting.

The tunneling current I at a given bias voltage V can be expressed by

$$\mathrm{I(V)} \propto \int_{-\infty}^{\infty}[f(E)-f(E+eV)]\,\rho(E)dE \qquad (1)$$

where f(E) is the Fermi function and ρ(E) is the density of state of sample. Then, we can obtain dI/dV by taking the derivative of Eq. (1)

$$\frac{\mathrm{dI}}{\mathrm{dV}}(\mathrm{V}) = A\int_{-\infty}^{\infty}\frac{d}{dV}[f(E+eV)]\,\rho(E)dE \qquad (2)$$

A is a constant. For a superconductor, ρ(E) is given by

$$\rho(E) = |E|/\sqrt{E^2-\Delta^2} \qquad (3)$$

where Δ is superconducting gap. If the effect of lifetime broadening is taken into calculation, ρ(E) can be derived in

$$\rho(E) = Re(|E-i\Gamma|/\sqrt{(E-i\Gamma)^2-\Delta^2}) \qquad (4)$$

where Γ is the energy of lifetime broadening. We fit the measured superconducting spectra with Eq. (2) and (4) by Levenberg-Marquardt method with three physical parameters: T_{eff} (effective temperature from Fermi function), Γ and Δ. The fitting is converged with Chi-square smaller than 10^{-9}. The fitting parameters in Fig. 5A are Δ_0 = 0.45meV, T_{eff} = 0.80K, Γ = 3.19x10^{-7}eV and A = 1.14.

For isotropic two s-wave gap fitting, the dI/dV can be expressed by the superposition of the contributions from the two gaps

$$\frac{\mathrm{dI}}{\mathrm{dV}}(\mathrm{V}) = X\frac{\mathrm{dI_1}}{\mathrm{dV}} + (1-X)\frac{\mathrm{dI_2}}{\mathrm{dV}} \tag{5}$$

where X is the ratio of two gaps and I_1 and I_2 are the tunneling current from Eq. (1) with different size of gap Δ_1 and Δ_2, respectively. The comparison between single and two gap fitting is shown in fig. S6B and fig. S6C.

Superconducting gap as function of temperature in the BCS theory can be approximately expressed as

$$\Delta(\mathrm{T}) = \Delta_0 \tanh(1.74\sqrt{(T_c/T)-1}) \tag{6}$$

where Δ_0 is the gap at zero temperature, and T_c is the critical temperature. T_c = 3.5K and Δ_0 = 0.45meV for Eq. (6) in Fig. 5C are determined from the measured dI/dV spectra.

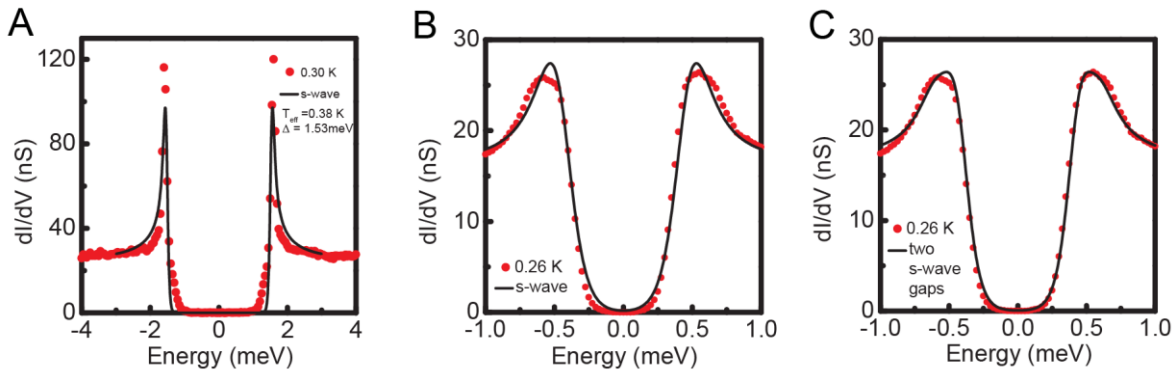

fig. S6. BCS fitting of superconducting tunneling spectrum. (**A**) The superconducting gap of Nb tip on Au (111). The black line is single gap fitting. (**B**) The single gap and (B) the isotropic two gap fitting of BCS theory with Δ_1 = 0.58meV, Δ_2 = 0.42meV. T_{eff} = 0.65K, Γ = 2.45x10^{-7}eV, A = 1.44 and X = 0.17. The spectrum is as same as which in Fig. 3A. Even if there exist two gaps, the magnitudes of two gaps would be similar by the fitting. Slight anisotropy in s-wave gap can also lead to the measured spectrum.

note S7. Comparison of normalized differential conductance at normal and superconducting states on a Pb-terminated surface.

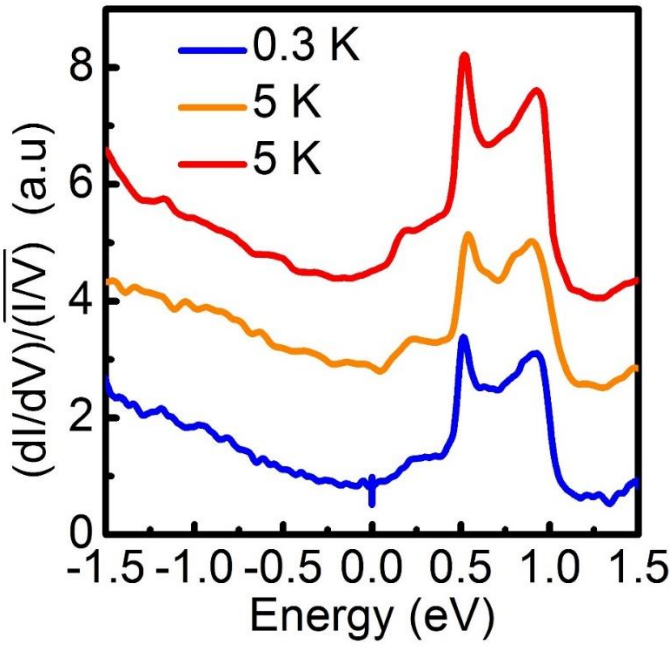

fig. S7. Normalized differential conductance taken on Pb-terminated surface. The orange and blue curves in the normal state were obtained on the same sample with the same tip by home-built ^{3}He STM, whereas the red curve in superconducting state was obtained by home-built cryogenic UHV SI-STM used for QPI measurements. The curves are equally shifted by 2a.u. for clarity. The only difference between three spectra is the opening of superconducting gap at E_F at T=0.3 K. The conductance is not zero at E=0 for superconducting spectrum due to the large modulation voltage. The two peaks originated from the TSSs at E~0.5eV and E~1.0eV persist when the TSSs become superconducting. (Setpoint V=800mV, I=1nA, lock-in modulation=0.5mV for blue STS curve; Setpoint V=1.4V, I=300pA, lock-in modulation=10mV for orange STS curve; Setpoint V=200mV, I=5pA, lock-in modulation=10mV for red STS curve.).

note S8. Upper critical field, lattice parameter of Abrikosov lattice, and normalized zero bias conductance of a vortex.

We use Ginzburg-Landau formula

$$\sigma(x,y,0) = \sigma_0 + (1-\sigma_0)(1-\tanh(\sqrt{(x-x_0)^2+(y-y_0)^2}/\sqrt{2}\xi))$$

for fitting zero bias conductance (ZBC) peak of vortex, where σ_0 is normalized ZBC away from the vortex core, x_0 and y_0 are the position of vortex core, and ξ is the coherence length. We obtained ξ= 54.2nm. By using Ginzburg-Landau equation, the upper critical field $H_{c2}(T)=\Phi_0/2\pi\xi^2(T)$ (Φ_0 is the magnetic flux quantum), $H_{c2}(T)$ for field perpendicular to *ab* plane is 0.082 T at 0.26 K. The magnetic field dependence of the vortex core distance between nearest neighbors is shown in fig. S8A. In fig. S8B, the extrapolation of linear fit of normalized ZBC under different field exhibits H_{c2} =0.087 T.

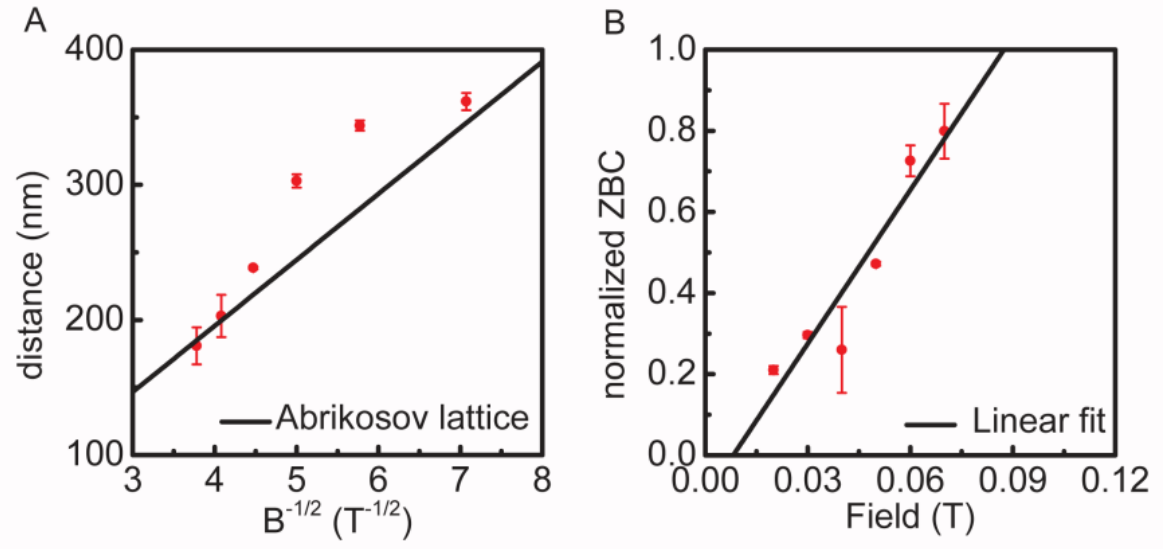

fig. S8. Magnetic field dependence of superconducting vortex lattice and vortex bound states. (**A**) The vortex core distance to the nearest neighbor D at different field B. Black line is the lattice constant for theoretical Abrikosov vortex $D = \sqrt{2\Phi_0/\sqrt{3}B}$. (**B**) σ_0 at different magnetic field with the linear fitting.

note S9. Spatial distribution of the superconducting gap on a Pb-terminated surface.

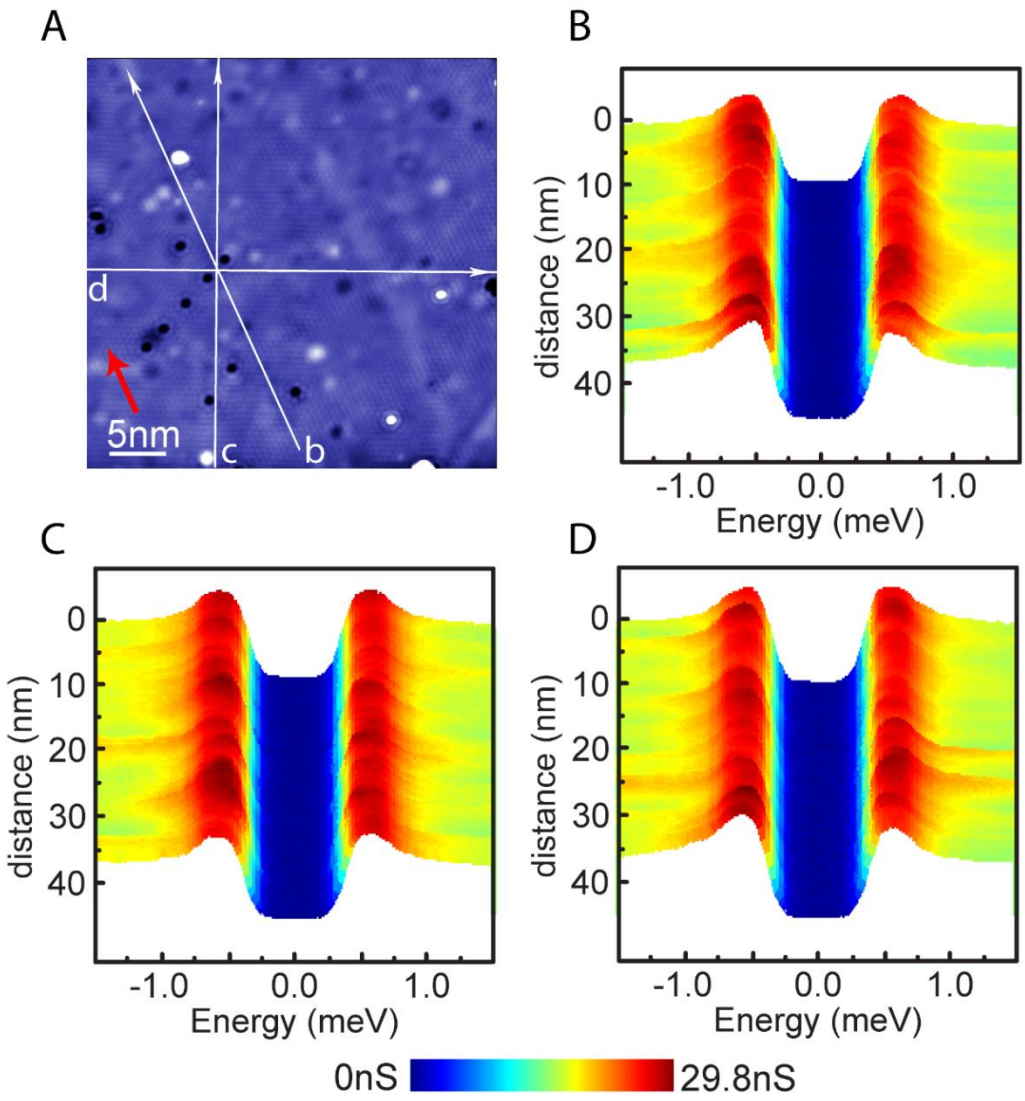

fig. S9. Homogenous superconducting gap on a Pb-terminated surface. (**A**) Topography taken at 0.26K on Pb-terminated surface. (V_s=10mV, I_s=60pA) (**B-D**) The distance dependence of superconducting gap at 0.26K. Each figure is containing 280 dI/dV spectra. The white alphabet b, c and d in fig. S9A represent the linecut of superconducting gap in fig. S9B-S9D, respectively. The white arrow in fig. S9A points out the direction. The red arrow points out the crystal orientation.

note S10. Topographic images and parameters of differential conductance maps on a Pb-terminated surface.

To better resolve the smaller q-vector with increasing energy, it is necessary to scan larger field of view (FOV) in real space accordingly, which allows us to zoom in the q-space around q=0 and subsequently enhance the q-resolution. Nevertheless, the setpoint of maps needs to be different in a large energy range due to the drastic increasing of density of states over 0.5 eV. Below, we draw a table to show the parameters, the simultaneous topographic images, FFT and the corresponding high resolution topographic images of differential conductance maps.

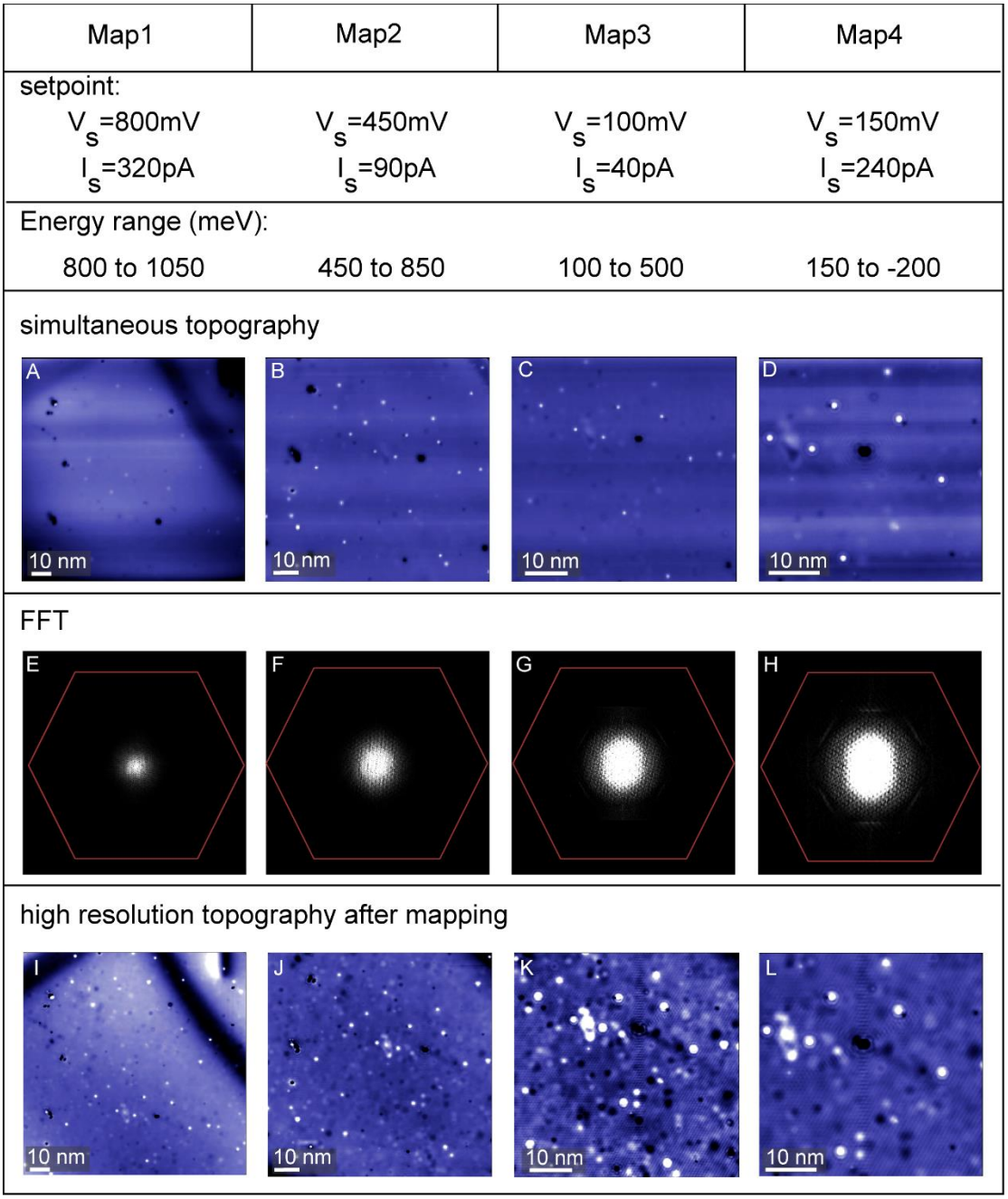

fig. S10. Topographic images of differential conductance maps on the Pb-terminated surface. (**A-D**) The simultaneous topography of different maps. (**E-H**) The FFT of fig. S10A-S10D, respectively. (**I-L**) The high resolution topograhy for scale and share calibration is taken after mapping from the FOV of different maps. The red hexagon indicates the full Brillouin zone.

note S11. Setpoint effect of normalized differential conductance maps on a Pb-terminated surface.

The setpoint effect can distort the true physical quantity. We compared different normalized differential conductance maps extracted from Map 1-4 (S10) at the overlapped energy below and found no extra different signal.

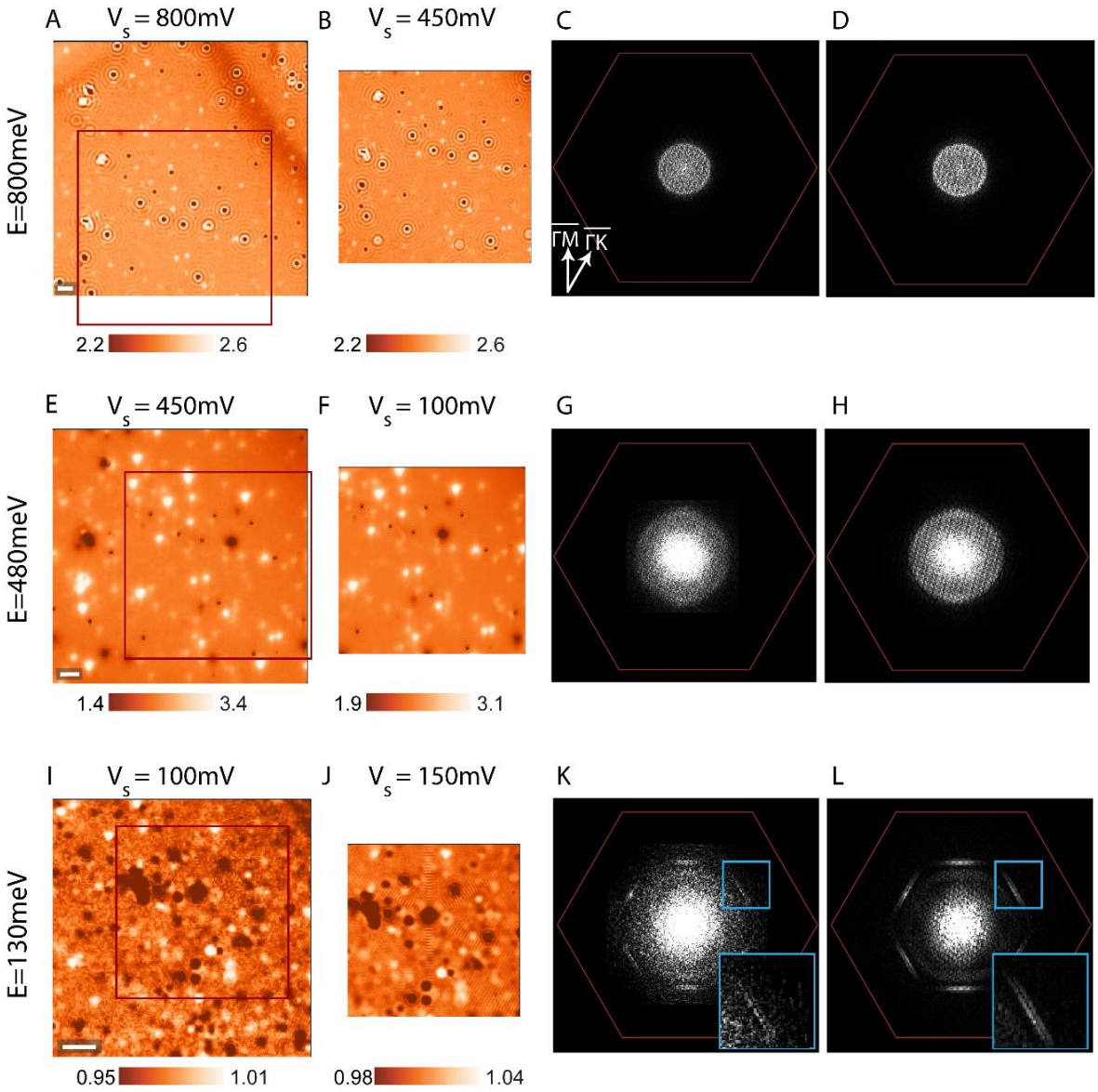

fig. S11. Bias independence of LDOS mapping and QPI imaging. (**A**, **B**), (**E**, **F**), (**I**, **J**) The normalized differential conductance maps from different setpoint bias V_s at overlapped energy. The scale bar in fig. S11 (A, E, I) each represents 10 nm. The red square in the fig. S11 (A, E, I) represents the same area of fig. S11 (B, F, **J**), respectively. (**C**, **D**, **G**, **H**, **K**, **L**) The FFT of fig. S11 (A, B, E, F, I, J), respectively.The red hexagon indicates the full Brillouin zone. All data are raw data with linear color scale.

note S12. Raw Fourier transform of normalized differential conductance maps on a Pb-terminated surface.

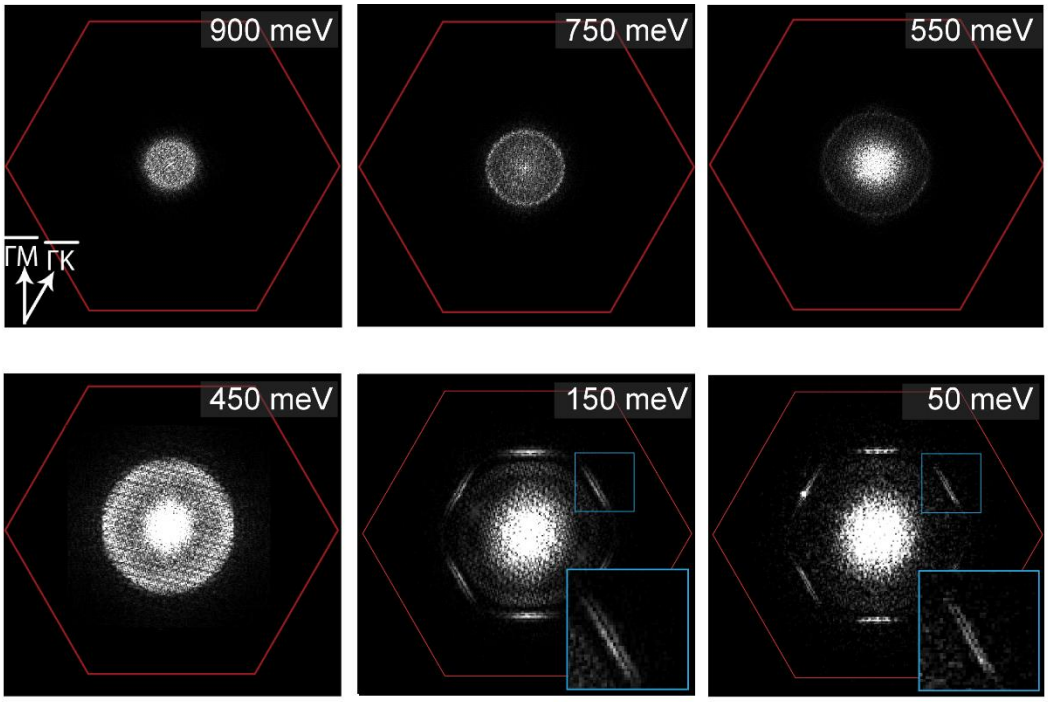

fig. S12. Raw data FFT of normalized differential conductance maps. The red hexagon indicates the full Brillouin zone. The data in Fig. 3 are calibrated by the high resolution topography in fig. S10I-S10L. Then the non-period noise at center is suppressed and they are taken exponential to increase contrast.

note S13. Differential conductance map at Fermi energy.

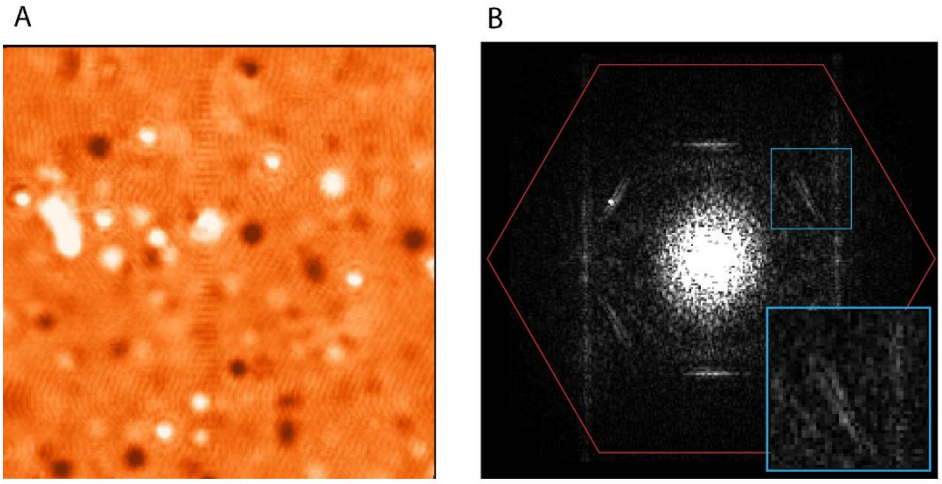

fig. S13. Visualization of QPI at Fermi energy. (**A**) Differential conductance map in a 44 nm FOV at Fermi energy. (**B**) The FFT of differential conductance map at Fermi energy. The red hexagon indicates the full Brillouin zone. All data are raw data with linear color scale.